Desalination and Water Treatment
www.deswater.com

doi: 10.5004/dwt.2022.28350

254 (2022) 94–103
April

Enhanced photocatalytic activity of α-Fe_2O_3/g-C_3N_4 composite materials for degradation of toluene in aqueous solution under visible light irradiation

Said Al Mamari[a], Singaravadivel Thangavel[b], Younghun Kim[c,*], Rengaraj Selvaraj[a,*]

[a]*Department of Chemistry, College of Science, Sultan Qaboos University, Al Khoudh, P.O. Box: 36, P.C. 123, Sultanate of Oman, emails: rengaraj@squ.edu.om/srengaraj1971@yahoo.com (R. Selvaraj), Said_2111@hotmail.com (S. Al Mamari)*
[b]*CAARU, College of Science, Sultan Qaboos University, Al Khoudh, P.O. Box: 36, P.C. 123, Sultanate of Oman, email: singh@squ.edu.om (S. Thangavel)*
[c]*Department of Chemical Engineering, Kwangwoon University, Seoul, Republic of Korea, email: Korea1@kw.ac.kr (Y. Kim)*

Received 18 January 2022; Accepted 17 February 2022

ABSTRACT

The photocatalytic oxidation method can be used to effectively remove volatile organic compounds present in water and has the ability to degrade even at low concentrations. This study presents the analysis of photoexcited charge carriers with a proposed Z-scheme interface of the α-Fe_2O_3/g-C_3N_4 composite for better photocatalytic degradation of toluene in aqueous solution. The α-Fe_2O_3/g-C_3N_4 heterojunction synthesized by the solvothermal method by combining α-Fe_2O_3 microspheres constructed from several nanospheres with g-C_3N_4 nanosheets. The prepared samples were characterized by different techniques such as X-ray diffraction, Fourier-transform infrared spectroscopy, X-ray photoelectron, scanning electron microscopy, energy-dispersive X-ray spectroscopy, high-resolution transmission electron microscopy, UV-Vis diffuse reflectance spectroscopy, and photoluminescence in order to analyze their elemental composition and optical properties. The degradation of toluene as a volatile organic compound candidate is analyzed to determine the photocatalytic efficiency. It is observed that narrowing the band gap in the hetero-composite structure increases the charge carrier mobility and reduces the recombination rate. Furthermore, the electrons migrate from the conduction band of α-Fe_2O_3 to the valence band of g-C_3N_4 due to the shift in the interfacial interaction band position. The 60% α-Fe_2O_3/g-C_3N_4 composite exhibits the highest photocatalytic activity among all samples and more than 90% degradation of toluene in water is achieved.

Keywords: α-Fe_2O_3; g-C_3N_4; Photocatalyst; Toluene; Degradation; Visible light; Water treatment

1. Introduction

Extensive research has been conducted in recent years on improving the structural and textural properties of semiconductor nanomaterials for the generation of renewable energy and for environmental conservation [1,2]. New and efficient methods for the degradation of organic pollutants for water treatment have been developed for the purification of public and industrial emissions [3]. Photocatalysis is the acceleration of a reaction carried out by a photocatalyst to generate electron-hole pairs. The mechanism of photocatalysis involves donation and acceptance of electrons and degradation of organic pollutants and becoming extremely hot research area. [4]. Semiconductor photocatalytic compounds

* Corresponding authors.

are widely used for the degradation of organic pollutants owing to the charge transfer and their capability to harvest ultraviolet or visible light [5]. Using semiconductor based photocatalysts for wastewater treatment are useful technology, due to ability for light (UV of visible) harvesting that generates electrons and holes pairs, which react with O_2 or OH anions to form powerful reactive species like superoxide and hydroxyl radicals [6].

Volatile organic compounds (VOCs) produced by gas combustion in petroleum industries are toxic and can pollute the environment. For instance, the accumulation of toluene in the adipose tissues, liver, and brain can produce carcinogenic effects when it enters through the lungs or the skin, and can result in building syndrome, nervous depression, and sometimes death [7]. Several techniques, such as photocatalytic oxidation, chemical oxidation, and adsorption/desorption methods, have been used to control the effects of VOCs. Among these, photocatalytic oxidation (PCO) is a notable technique for the removal of VOC and has the ability to degrade even at low concentrations; it presents several advantages such as mild working conditions, environmental conservation, high catalytic performance, and cost-effectiveness [8].

In recent years, graphitic carbon nitride, g-C_3N_4, has been identified as an effective photocatalyst material which can be employed in water splitting and for removing pollutants, owing to its high conductivity, non-toxicity, and chemical stability. Polymeric semiconductors have an appropriate band gap of 2.7 eV, which can enable the absorption of blue light up to 450 nm [9]. However, they face drawbacks such as low specific surface area, fast charge recombination, and a minimal number of active sites [10,11]. Due to that, many researchers focused to overcome the such disadvantages by using defective bulk g-C_3N_4 that could lead to lattice distortions to narrow the band gap, generating sub gap and significantly enhance the solar light utilization [12]. The modification of the g-C_3N_4 nanosheets by Ru particles with facial and green method, enhanced the rapid separation of the electron-hole pairs which increased the photocatalytic activity and selectivity as well [13]. Additionally, another way to solve the problem can be resolved by coupling with other semiconductors such as TiO_2, ZnO, and α-Fe_2O_3, thus improving the charge carrier rate, increasing the separation of photoexcited electrons and holes, and enhancing the photocatalytic performance [10–16]. Furthermore, coupling g-C_3N_4 can narrow down the band gap, forming a Z-scheme heterojunction, resulting in the expansion of light harvesting with a significant variation in the electron band structure [17].

Hematite (α-Fe_2O_3) is a visible light transition metal oxide and an n-type semiconductor with a band gap of 2.0–2.2 eV, which can utilize and absorb visible light of a wavelength of up to 600 nm. It is the most stable phase when compared to other iron oxides, while being cost-effective and environmentally friendly [18,19]. The potentials of the valance and conductive band edges of g-C_3N_4 are observed to be approximately 1.57 and 1.13 eV, respectively [20,21]. Meanwhile, the potentials of the two band edges of α-Fe_2O_3 are close to 0.28 and 2.48 eV [22]. Therefore, the covenant positions of the valance and conductive bands in g-C_3N_4 and α-Fe_2O_3 can enable the formation of a Z-scheme photocatalyst.

This study presents the synthesis of α-Fe_2O_3/g-C_3N_4 composites through the thermal treatment of melamine as a precursor to prepare the g-C_3N_4 compound followed by the solvothermal method with an iron chloride hexahydrate precursor to prepare the heterojunction structure. The prepared materials are analyzed for the degradation of toluene in aquatic media using photocatalytic oxidation and adsorption under irradiation using a white LED lamp as a visible light source. The possible photocatalytic reaction mechanism of the composites for toluene degradation is also proposed.

2. Experimental

All the reagents were purchased from Sigma-Aldrich (analytical grade) and used without further purification. Iron(III) chloride hexahydrate ($FeCl_3{\cdot}6H_2O$) was used as the iron oxide precursor, melamine as the graphitic-like carbon nitride precursor, ethanol (C_2H_6O) as the solvent, and toluene (C_7H_8) as the VOC pollutant.

2.1. Preparation of g-C_3N_4, Fe_2O_3 and its composite materials

The graphitic carbon nitride was prepared by using 1.0 g of melamine precursor placed in a crucible with a cover heated to 550°C for 3 h at a heating rate of 20°C/min in the muffle furnace under atmospheric conditions. The single metal oxide was prepared by adding 0.5 g of $FeCl_3{\cdot}6H_2O$ to 20 mL of ethanol and stirred for 1 h. The solution was then transferred to a Teflon-lined stainless-steel autoclave, which was heated to 160°C for 12 h at a heating rate of 3°C/min. Later, the suspension was aged for a day to settle down the precipitate then, centrifuged and washed three times with ethanol. After that, the precipitate was dried at 80°C for 3 h and calcinated at 450°C for another 3 h at a heating rate of 3°C/min.

The α-Fe_2O_3/g-C_3N_4 composite was fabricated as follows. 160 mg of g-C_3N_4 dispersed in 20 mL of ethanol, and stirred for 30 min. Subsequently, 40 mg of α-Fe_2O_3 precursor was added to a conical flask containing 20 mL of ethanol and stirred for 30 min. The two solutions were then mixed and stirred for 1 h; the mixture was transferred to a Teflon-lined stainless-steel autoclave and the solvothermal steps were followed as explained earlier. The amount of α-Fe_2O_3 coupled with g-C_3N_4 was varied with mass ratios of 20%, 40%, and 60% to obtain the composites of 20% α-Fe_2O_3/g-C_3N_4, 40% α-Fe_2O_3/g-C_3N_4 and 60% α-Fe_2O_3/g-C_3N_4, respectively.

2.2. Characterization of the photocatalysts

Fourier-transform infrared (FTIR) spectra were obtained in the range of 4,000–400 cm^{-1} using a Bruker FTIR Alpha (ECO-ART) spectrometer. X-ray powder diffraction using a Panalytical X-ray diffractometer (Model: X'Pert Pro) with Cu Kα radiation (l = 1.54 Å) was used to analyze the crystallinity of the g-C_3N_4, α-Fe_2O_3 and α-Fe_2O_3/g-C_3N_4 samples. An accelerating voltage of 45 kV and an emission current of 40 mA were employed. The morphologies of the samples were analyzed using a field emission scanning electron microscope (FE-SEM, JSM-7800F JOEL, Japan)

with a maximum working voltage of 30 kV, a resolution of 0.8 nm, and a working distance of 10 nm. Similarly, the nanostructures were characterized using a field emission transmission electron microscope (FE-TEM, JEM-2100F JEOL, Japan) with a maximum working voltage of 200 kV, a resolution of 0.1 nm, and 1.5-million-time magnification. Multiprobe photoelectron spectroscopy (Omicron Nanotechnology, Germany) was used to obtain the X-ray photoelectron spectra (XPS) of the samples. Particularly, monochromatic Al Kα radiation ($h\nu$ = 1486.6 eV) was generated at 15 kV and an emission current of 20 mA. The individual element peaks were indicated at 20 eV by a wide scan from a constant analyzer transition energy of 50 eV. The charge composition was evaluated by flooding with electrons since the charging of the non-conducting samples in the XPS analysis is inevitable. The obtained XPS spectra were further deconvoluted into individual components using a Gaussian Lorentzian function, and the Casa XPS software program (Casa Software Ltd., UK) was used to subtract the background from the Shirley function. Furthermore, the binding energies were calibrated with respect to the transverse C 1s which is observed at 284.6 eV. The UV-Visible DRS spectra were recorded using a Shimadzu (UV-2600i) UV-vis spectrometer with $BaSO_4$ applied as the standard sample. The photoluminescence (PL) spectra were obtained using a SCINCO (FS-2) fluorescence spectrofluorometer.

2.3. Photocatalytic activity studies

Toluene is a type of VOC which was selected as a candidate pollutant to test the photocatalytic activity of the synthesized pure and composite samples for the degradation of VOCs present in water. All the experiments were carried out in a photocatalytic reactor batch system made of a cylindrical borosilicate glass reactor vessel (250 mL). The reactor has outer jacket which allows the water for cooling the reactor the photodegradation process. The LED lamp (50 W) was positioned in the reactor for illumination. Firstly, an air diffuser equipped in the reactor was used to disperse oxygen into the solution. The prepared sample (100 mg) was then added to 250 mL of an aqueous toluene solution with an initial concentration of 10 mg/L. The solution was magnetically stirred for 30 min in the dark before being exposed to illumination in order to ensure the adsorption and desorption equilibrium between the prepared photocatalyst and the toluene. During illumination, 7 mL of aliquots of the solution were taken from the reactor at scheduled time intervals.

The photocatalytic degradation of toluene was quantified by gas chromatography with a flame ionization detector (GC-FID). The GC model (Agilent 7890A-GC, Agilent-7697A HSS Loop) headspace sampler with a loop size of 1 mL was used in the static-loop headspace mode for sample introduction. Effluent from the HS-20 was split in a ratio of 20:1, and then divided to two identical columns using a 3-way "T" fitting approach. The outlet ends of the two columns were connected to the FID detectors, which heated the sample up to 150°C in the presence of air (400 mL/min) followed by carrier gases, H_2 (40 mL/min), and helium (30 mL/min).

3. Results and discussion

3.1. FTIR analysis

Fig. 1 presents the FTIR of pure g-C_3N_4, pure α-Fe_2O_3, and their composite to analyze the interactions between the two materials. The intense absorption peak at 809 cm^{-1} is attributed to the tri-s-triazine rings in the pure g-C_3N_4. Also, absorption band at 1,320 and 1,421 cm^{-1} are attributed to the stretching vibrations of C–NH–C bridges. Further, the peaks at 1,412 and 1,634 cm^{-1} are assigned to the vibration of C–N and C=N in the aromatic ring. Meanwhile, the absorption vibration mode observed around 3,150 cm^{-1} could be attributed to the –NH group of g-C_3N_4 and represented by the broad band at 3,650–3,000 cm^{-1}, which caused by overlapping of OH stretching group arises from water adsorption [6,23]. Additionally, the peak at 538 cm^{-1} indicates the stretching vibration mode of Fe–O in the pure α-Fe_2O_3 particles [24]. The FTIR spectra of the 60% α-Fe_2O_3/g-C_3N_4 composite are comparable with the g-C_3N_4 peaks, which decrease in intensity with increasing amounts of α-Fe_2O_3 in the composite. The FTIR peaks of the composites are shifted to higher wavenumbers than those of pure g-C_3N_4 owing to the strong interfacial interaction between g-C_3N_4 and α-Fe_2O_3.

3.2. X-ray diffraction analysis

X-ray diffraction (XRD) analysis was used to analyze the crystalline phases and the formation of the pure g-C_3N_4, pure α-Fe_2O_3, and their composites, as depicted in Fig. 2. The XRD pattern of pure g-C_3N_4 exhibits a weak diffraction peak at 13.0° and a strong peak at 27.5°. These peaks are indexed to the (100) and (002) diffraction planes of g-C_3N_4 (JCPDS 87-1526) [25], respectively. The XRD pattern of pure α-Fe_2O_3 exhibits diffraction peaks at 24.4°, 33.2°, 35.7°, 40.1°, 49.6°, 54.2°, 62.6°, and 64.1°, which correspond to the (JCPDS 89-0596) [26] index planes, (012), (104), (110), (113), (024), (116), (112), (214), and (300), respectively. For the coupled α-Fe_2O_3/g-C_3N_4 composites, both phases of the iron oxide and the g-C_3N_4 are observed in the powder XRD peaks depicted in Fig. 2c and d. However, the prepared

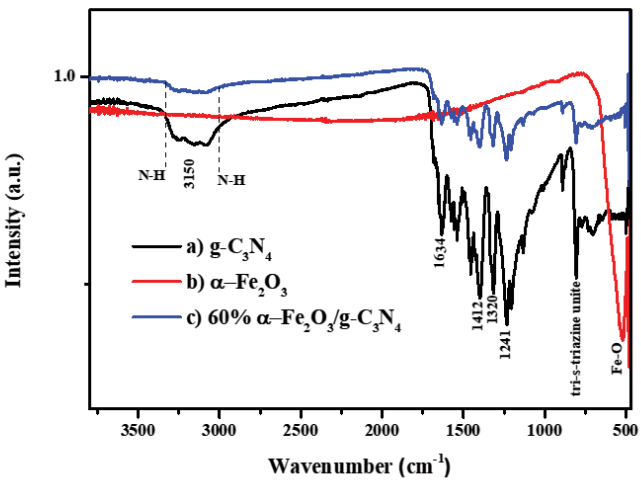

Fig. 1. FTIR spectra of (a) pure g-C_3N_4, (b) pure α-Fe_2O_3 and (c) 60% α-Fe_2O_3/g-C_3N_4 composite.

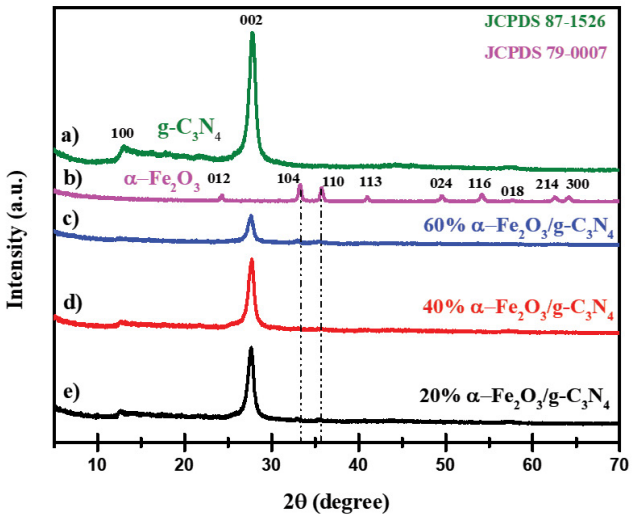

Fig. 2. XRD patterns of (a) pure g-C_3N_4, (b) pure α-Fe_2O_3, (c) 60% α-Fe_2O_3/g-C_3N_4, (d) 40% α-Fe_2O_3/g-C_3N_4, and (e) 20% α-Fe_2O_3/g-C_3N_4 composites.

composites demonstrated a decrease in the diffraction peak intensity of g-C_3N_4 with the extra loading of α-Fe_2O_3. This indicates the successful formation of the two-phase composite without any impurity peaks in the 20% α-Fe_2O_3/g-C_3N_4, 40% α-Fe_2O_3/g-C_3N_4, and 60% α-Fe_2O_3/g-C_3N_4 compounds.

The Scherrer equation [27] was used to estimate the average grain size (D) of the reflection planes of the samples as follows:

$$D = \frac{\kappa\lambda}{\beta_{hkl}\cos\theta_{hkl}} \quad (1)$$

where κ denotes the shape factor, λ denotes the X-ray wavelength, β_{hkl} is the full width at half maximum (FWHM) of the diffraction peak in radian, and θ_{hkl} denotes the Bragg angle. The average crystallite sizes of the pure g-C_3N_4 and pure α-Fe_2O_3 were calculated to be 36.3 and 22.7 nm, respectively. The average crystallite sizes for 20%, 40% and 60% of α-Fe_2O_3/g-C_3N_4 composites, were found to be 37.8, 41.1 and 34.9 nm, respectively.

3.3. Morphology analysis

The morphologies of the pure g-C_3N_4, pure α-Fe_2O_3, and α-Fe_2O_3/g-C_3N_4 composites were analyzed through scanning electron microscopy (SEM). Fig. 3a illustrates the sheet-like structure of g-C_3N_4, and Fig. 3b and c demonstrate that the α-Fe_2O_3 sample comprises a microsphere composed of several nanosphere particles. Furthermore, the fabrication of α-Fe_2O_3 in the presence of g-C_3N_4 does not alter the spherical structure of α-Fe_2O_3, as shown in Fig. 3d. Transmission electron microscopy (TEM) and high-resolution high-resolution transmission electron microscopy (HR-TEM) were used to characterize the morphologies and microstructures of the prepared samples. Fig. 4a and b illustrate the TEM image of the pure g-C_3N_4 nanosheets with a wrinkled two-dimensional structure. Similarly, the TEM images present pure α-Fe_2O_3 microspheres with small nanoparticle spheres (Fig. 4c). Furthermore, the TEM images of 20% α-Fe_2O_3/g-C_3N_4 depict the presence of the α-Fe_2O_3 microspheres on the surface of the g-C_3N_4 nanosheets with an average size of 100 nm, indicating a close interface between the two materials in the composite (Fig. 4d and e). Consequently, the photogenerated charge carriers and electron–hole separation was enhanced. Energy-dispersive X-ray (EDX) analysis was performed to determine the elemental composition of the prepared composite, and the results are presented in Fig. 5a. The composite sample comprises four elements: C, N, Fe, and O, which can further confirm the high purity of the 20% α-Fe_2O_3/g-C_3N_4 composite structure. Furthermore, the elemental mapping analysis was performed to analyze the elemental distribution of the iron(III) oxide particles on the surface of the g-C_3N_4 nanosheets; the results are presented in Fig. 5b. The scanned area shows Fe and O, where α-Fe_2O_3 is located in the presence of C and N over the examined area. The quantification of the scanned area verified the presence of iron and oxygen, where the α-Fe_2O_3 particles were located. Additionally, a high ratio of C and N are observed in most of the scanned area.

3.4. XPS analysis

XPS was performed to determine the elemental composition and chemical states; Fig. 6 presents the XPS results for pure g-C_3N_4, pure α-Fe_2O_3, and the 60% α-Fe_2O_3/g-C_3N_4 composite. The XPS survey spectra revealed that the primary elements were C, N and medium concentrations of Fe and O. Following calibration, the binding energy for g-C_3N_4 is located at 396 and 395.2 eV for the mine (N 1s) peak and at 284.8 eV for the C 1s peak, as shown in the high-resolution C 1s in Fig. 6c [28,29]. The O 1s spectrum presents a characteristic peak of α-Fe_2O_3 at 528.7 eV, which is matching with 60% α-Fe_2O_3/g-C_3N_4 composite but, shifted to a lower binding energy as it showed in Fig. 6e. Meanwhile, C 1s and N 1s are shifted to a higher binding energy. Additionally, the Fe $2p^{3/2}$ and Fe $2p^{1/2}$ spectra of α-Fe_2O_3 have two peaks at 710.9 and 724.1 eV, respectively [30]. However, the two states were shifted to lower binding energies in the 60% α-Fe_2O_3/g-C_3N_4 sample, as depicted in Fig. 6f. This can be attributed to the interaction between the α-Fe_2O_3 particles and the g-C_3N_4 nanosheet layers in the heterojunction of the α-Fe_2O_3/g-C_3N_4 composite.

3.5. UV-Vis diffuse-reflectance spectrum study

UV-Vis diffuse reflectance spectroscopy (UV-DRS) was used to analyze the optical properties and band transitions of the prepared samples, as shown in Fig. 7a. The pure g-C_3N_4 sample shows an absorption edge at approximately 442 nm [31], while the α-Fe_2O_3 sample shows a strong absorption in the UV to visible region within the absorption edge lower than 650 nm [32]. The absorption edges of the 20, 40, and 60% α-Fe_2O_3/g-C_3N_4 composites were distributed between those of the g-C_3N_4 and α-Fe_2O_3 composites. However, the 60% α-Fe_2O_3/g-C_3N_4 composite exhibited higher absorption than the other composites, which can be attributed to the increase in the interaction between the g-C_3N_4 and α-Fe_2O_3

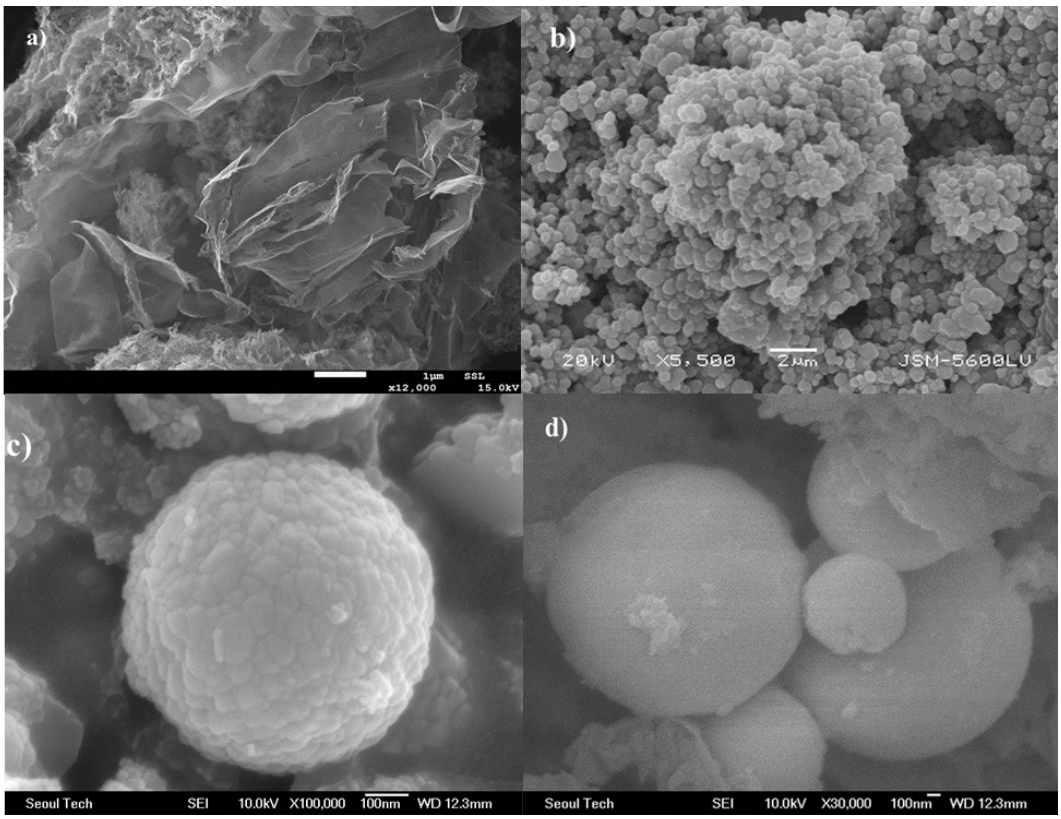

Fig. 3. SEM images of (a) pure g-C_3N_4, (b, c) pure α-Fe_2O_3, and (d) 20% α-Fe_2O_3/g-C_3N_4 composite.

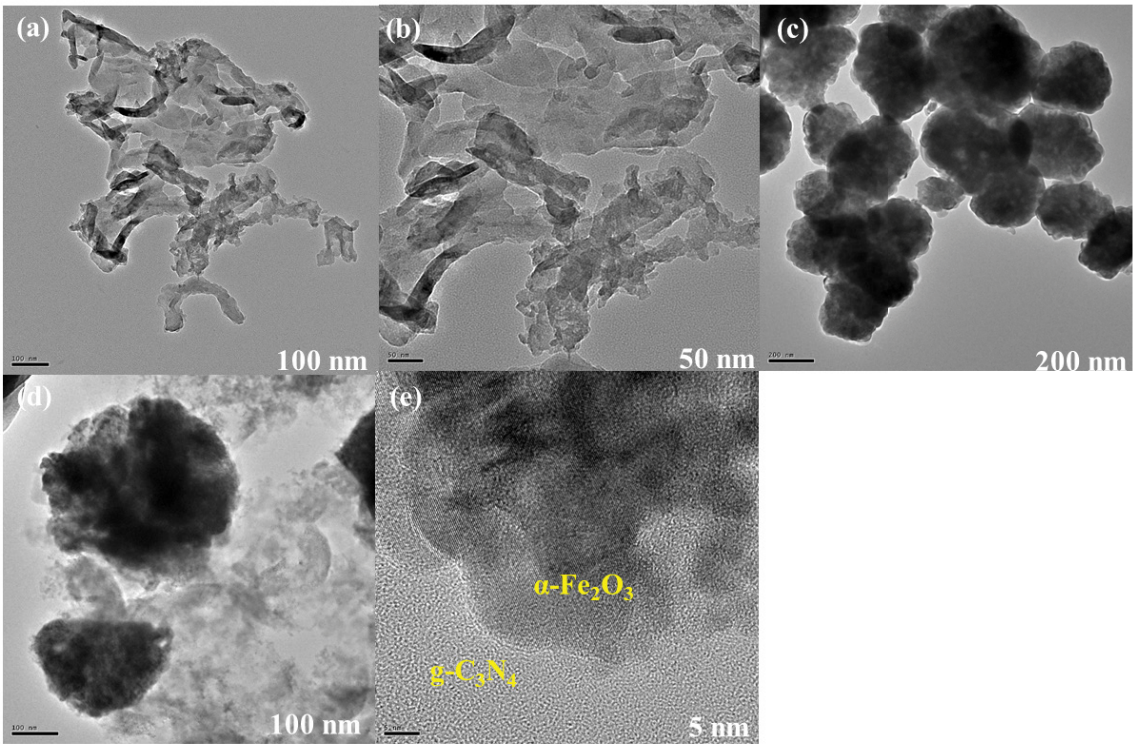

Fig. 4. TEM images of (a, b) pure g-C_3N_4, (c) pure α-Fe_2O_3, (d) 20% α-Fe_2O_3/g-C_3N_4 composite, and HR-TEM image of (e) 20% α-Fe_2O_3/g-C_3N_4 composite.

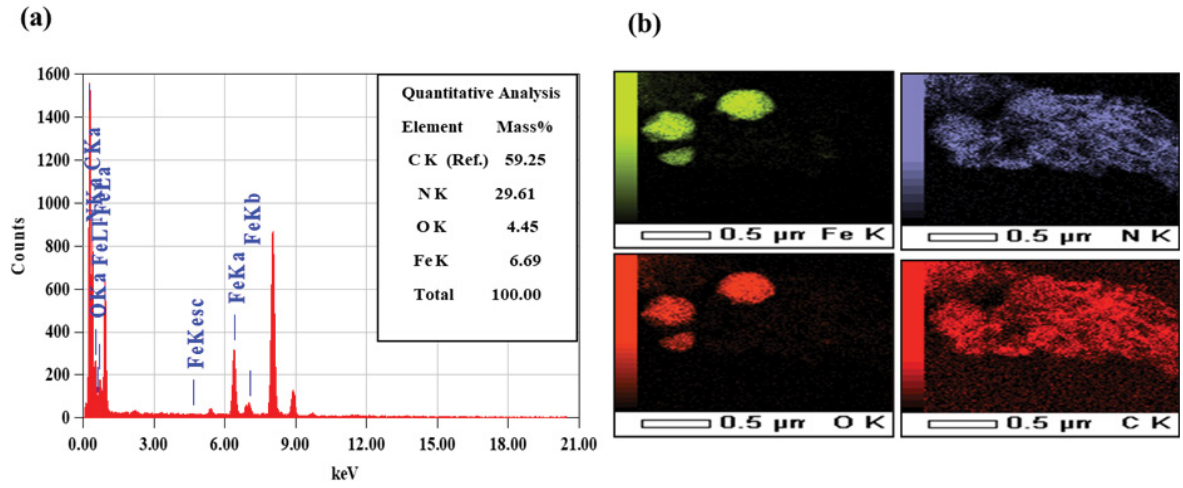

Fig. 5. (a) EDX and (b) elemental mapping of 20% α-Fe_2O_3/g-C_3N_4 composite.

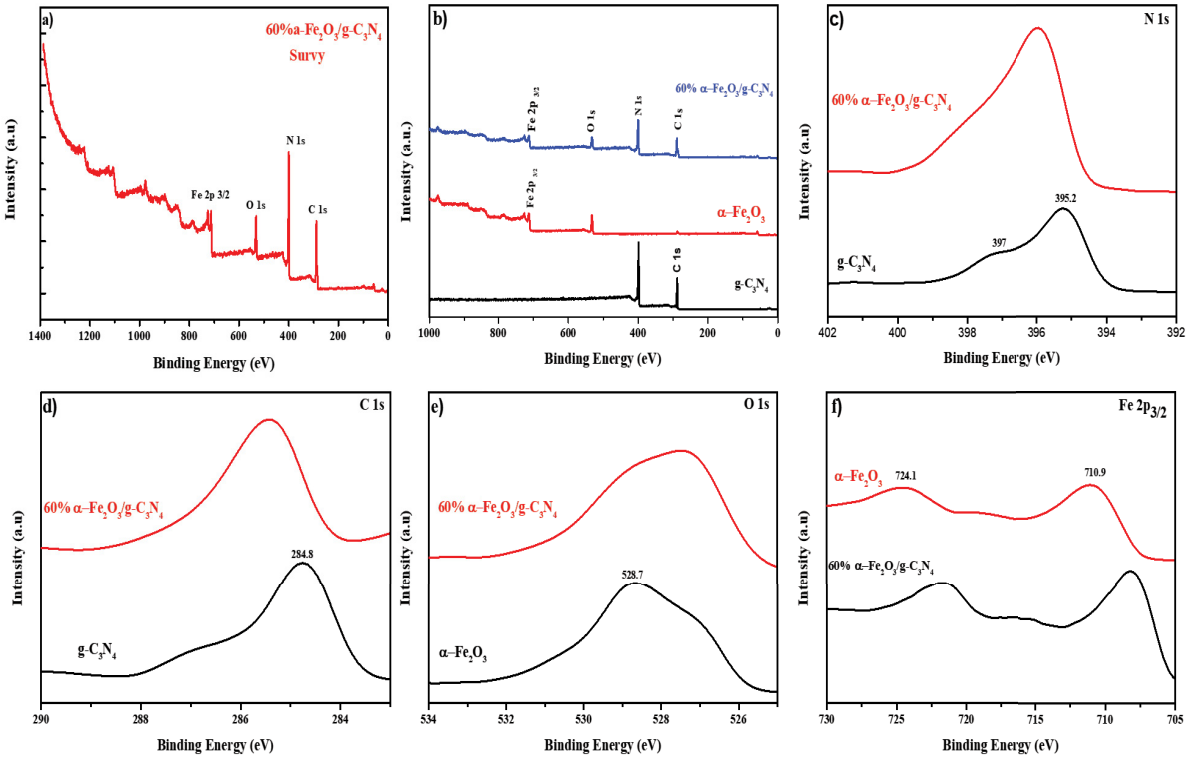

Fig. 6. XPS spectra of (a) survey in 60% α-Fe_2O_3/g-C_3N_4, (b) survey in g-C_3N_4, α-Fe_2O_3, and 60 α-Fe_2O_3/g-C_3N_4 samples, (c) N 1s, (d) C 1s, (e) O 1s, and (f) Fe 2p.

particles. The powder was changed from yellow to gray to red, when the two materials are coupled to form a composite, which improves the absorption in the visible region and enhances the interaction effect to increase the rate of charge carrier transfer and separation of the electron hole. The optical band gap energy of the samples can be calculated by using the Tauc equation [33] as follows:

$$\alpha h\nu = A\left(h\nu - E_g\right)^{n/2} \quad (2)$$

where α, h, ν, A, and E_g represent the absorbance coefficient, Plank constant, light frequency, proportionality, and band gap energy, respectively. The bandgap values depend on the electronic transitions of the semiconductor. Fig. 7b–e illustrate the band gaps in the g-C_3N_4, α-Fe_2O_3, 60% α-Fe_2O_3/g-C_3N_4, 40% α-Fe_2O_3/g-C_3N_4, and 20% α-Fe_2O_3/g-C_3N_4 composites, which are estimated to be 2.80, 2.04, 2.44, 2.62, and 2.77 eV, respectively. All the composites of α-Fe_2O_3/g-C_3N_4 present a lower band gap than pure g-C_3N_4 and a higher band gap than pure α-Fe_2O_3, which is close to the reported values [34,35].

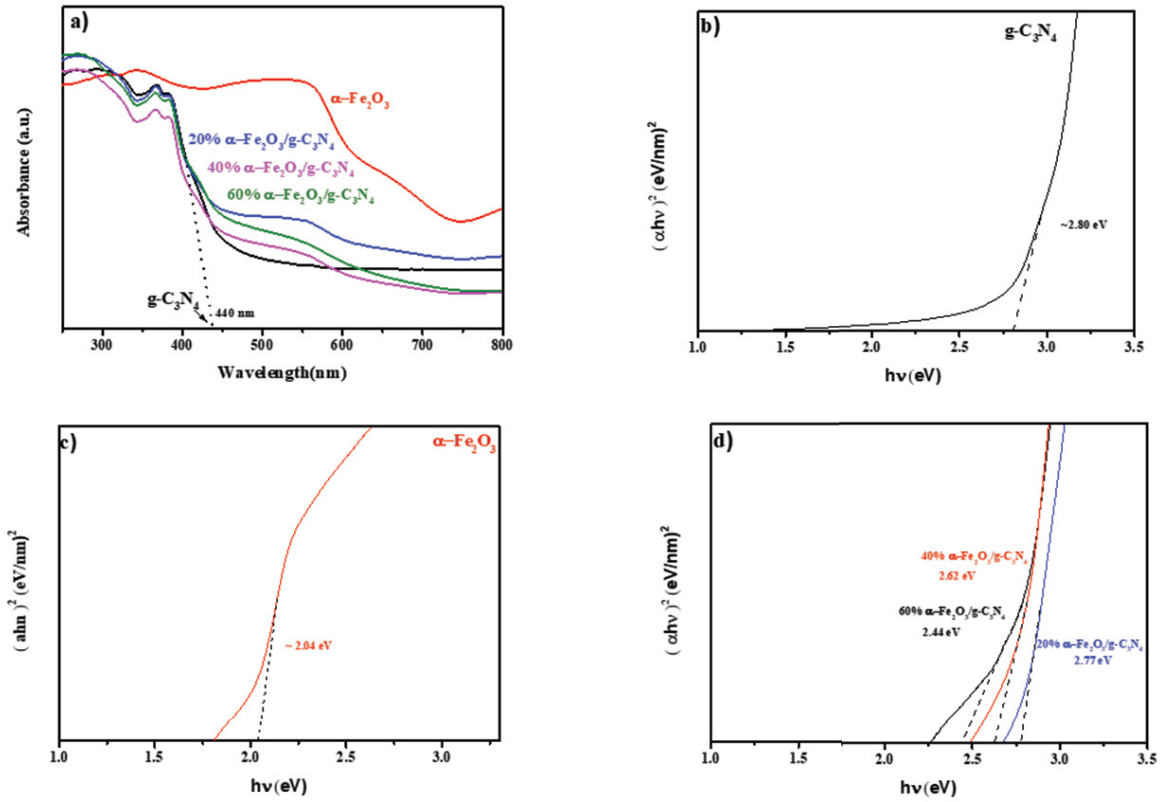

Fig. 7. (a) Absorption spectra of pure g-C_3N_4, pure α-Fe_2O_3, (b, c) absorption spectra of different α-Fe_2O_3/g-C_3N_4 composites and (d) Tauc plots for pure g-C_3N_4, pure α-Fe_2O_3 and α-Fe_2O_3/g-C_3N_4 composites.

3.6. Photoluminescence analysis

Photoluminescence spectroscopy (PL) can satisfy the optical properties of the heterostructure of the prepared semiconductor photocatalyst, presenting better separation of the photogenerated electron–hole pairs [36]. The peak emission of PL is caused by the recombination rate between the electrons and species holes on the surface of the photo-excited material. The intensity of the PL emission is directly proportional to the recombination rate of these pairs [37]. Fig. 8 presents the PL emission spectra of the prepared g-C_3N_4, α-Fe_2O_3, and α-Fe_2O_3/g-C_3N_4 composite samples after exposure to 320 nm light at room temperature. The first emission peak was observed at 437 nm, while no emission peak was observed for the α-Fe_2O_3 sample, which can be attributed to its low band gap (2.04 eV) energy. Additionally, the PL emission intensity was reduced from g-C_3N_4 after being coupled with the α-Fe_2O_3 microspheres, owing to the decrease in the photoexcited charge carrier recombination rate in the hetero-composite samples. Furthermore, the 60% α-Fe_2O_3/g-C_3N_4 sample presented the lowest PL emission when compared to the other samples, which demonstrates the strong synergistic effect between the surface of the g-C_3N_4 nanosheets and the iron oxide microspheres.

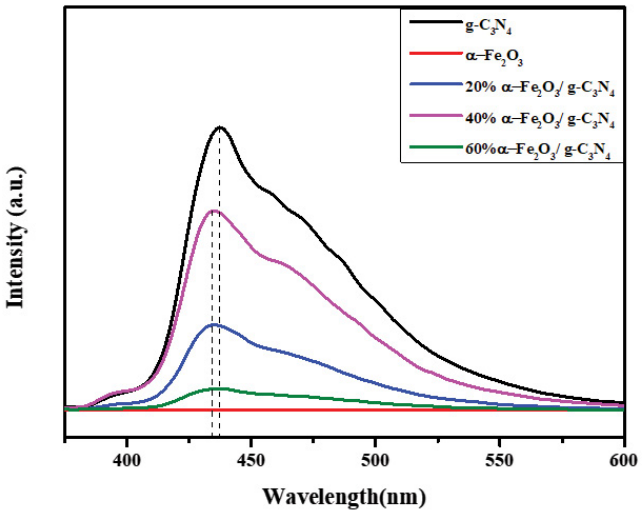

Fig. 8. PL spectra of the pure g-C_3N_4, pure α-Fe_2O_3 and α-Fe_2O_3/g-C_3N_4 composites.

3.7. Photocatalytic performance measurement

For the photocatalytic performance, the degradation of toluene was analyzed using the obtained α-Fe_2O_3/g-C_3N_4 samples under illumination by a 50 W power LED lamp, which was used as a visible light source (λ > 400 nm). 100 mg of the photocatalyst was added to a 250 mL toluene solution (10 mg/L). The mixture was kept in the dark for approximately 30 min to analyze the adsorption ability of the prepared catalyst. The reaction was then irradiated

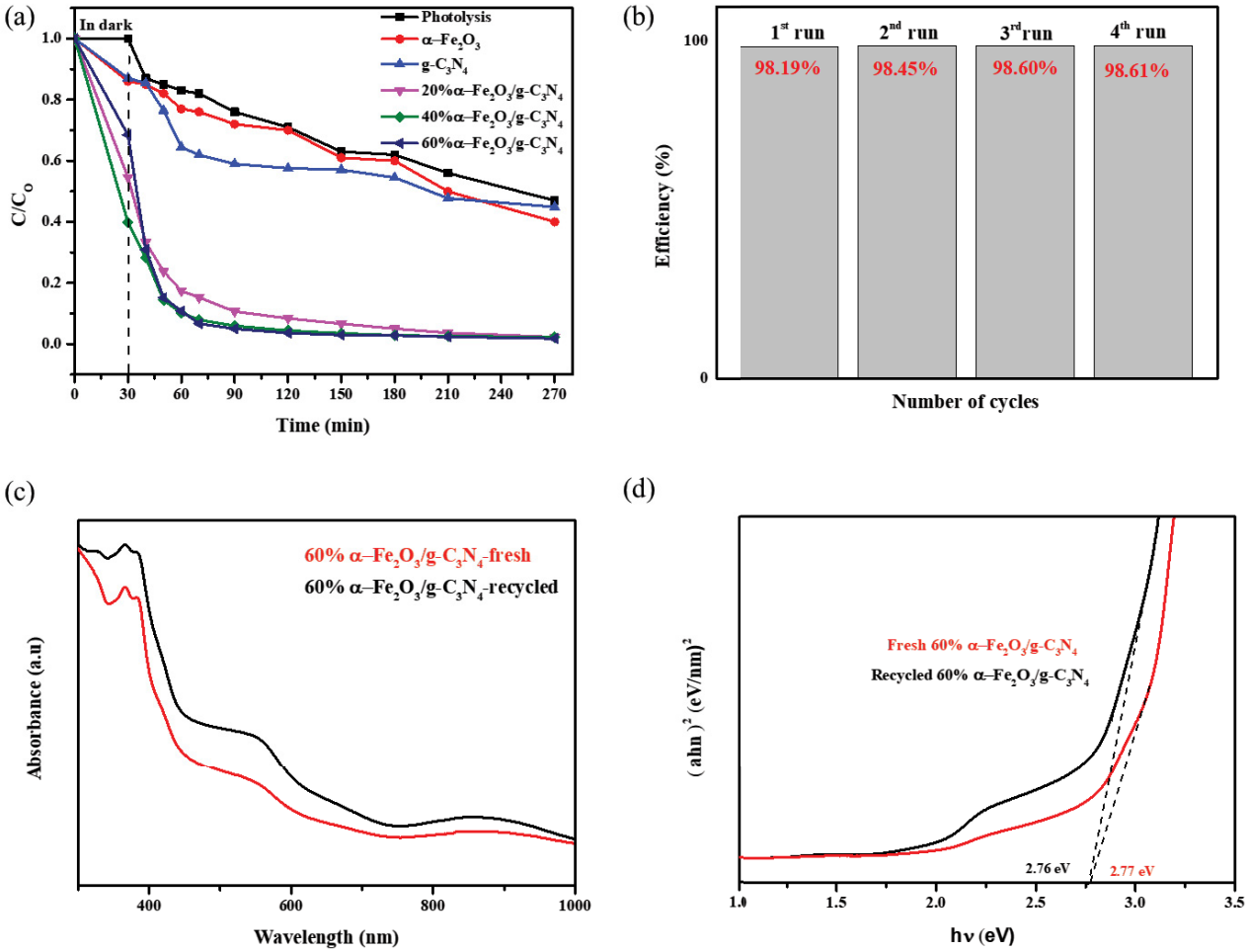

Fig. 9. (a) The degradation of toluene by g-C_3N_4, α-Fe_2O_3, and α-Fe_2O_3/g-C_3N_4 composites under visible light irradiation, (b) cycling runs for toluene degradation in the presence of 60% α-Fe_2O_3/g-C_3N_4 composite, (c) UV-Vis spectra and (d) Tauc plot for fresh and recycled 60% α-Fe_2O_3/g-C_3N_4 composite.

with visible light for 240 min under the passage of air to determine the photocatalytic performance. Furthermore, a control experiment was performed to determine the illumination of the VOC pollutant without the prepared photocatalyst. Fig. 9 illustrates the concentration change of toluene and 10 mg/L of toluene in an aqueous solution. A control experiment was conducted to determine the effect of illumination on the VOC compounds in the absence of the prepared photocatalysts. Moreover, the efficiency of the photocatalytic degradation producer was calculated by the following formula:

$$\text{Efficiency}(\%) = \left(\frac{C_0 - C}{C_0}\right) \times 100 \quad (3)$$

The pure g-C_3N_4 and α-Fe_2O_3 samples exhibited lower adsorption and photoactivity activities when compared to the coupled samples. The photodegradation ability of the α-Fe_2O_3/g-C_3N_4 samples was greater than that of the single-parent photocatalysts. The high performance of the composite is attributed to the modification of the morphology caused by the solvothermal process. Among all the samples, the 60% α-Fe_2O_3/g-C_3N_4 composite exhibited the highest photocatalytic degradation. This may be recognized by high interaction of the α-Fe_2O_3 particles on the surface on g-C_3N_4 nanosheets, which enhanced the number of charges carries and benefit the degradation process. Moreover, the stability of the 60% α-Fe_2O_3/g-C_3N_4 sample was determined by testing the photodegradation performance four times under the same conditions. The sample was washed, centrifuged, and dried at the end of each cycle and prior to use in the next cycle. Fig. 9b demonstrates the photodegradation efficiency of the 60% α-Fe_2O_3/g-C_3N_4 composite with high stability after the 4-cycles. Furthermore, the UV-Vis spectra and Tauc plot depicted in Fig. 9c and d demonstrate a small change in the absorption edge and band gap for the recycled 60% α-Fe_2O_3/g-C_3N_4 composite after 4-cycling when compared to the fresh sample. That would be attributed to the washing and drying treatment for the composite after each cycle.

3.8. Photocatalytic mechanism

Fig. 10 presents the possible band arrangement required to form the Z-scheme structure between g-C_3N_4 and α-Fe_2O_3.

From the UV-vis DRS analysis, the band gap of g-C_3N_4 and α-Fe_2O_3 are observed to be 2.80 and 2.04 eV, respectively. The conduction band edges can be estimated by using the following equations:

$$E_{CB} = X - E_C - 0.5E_g \quad (4)$$

where E_{CB} represents the conduction band edge potential, X denotes the electronegativity of the semiconductor (the X value for g-C_3N_4 is 4.72 and 5.825 eV for α-Fe_2O_3) [38,39], E_C is the energy of the free electrons on the hydrogen scale (4.5 eV), and E_g denotes the band gap energy. The valence band edge can be calculated using the following equation:

$$E_{VB} = E_{CB} + E_g \quad (5)$$

Therefore, the E_{CB} and E_{VB} of g-C_3N_4 are measured to be –1.18 and 1.62 eV, respectively. The conduction band (CB) and valence band (VB) edge potential of α-Fe_2O_3 are measured to be 0.305 and 1.735 eV, respectively.

Fig. 10 presents a proposed Z-scheme for the photocatalytic degradation of toluene over the α-Fe_2O_3/g-C_3N_4 composite and the band structure under visible-light irradiation. Electrons and holes are generated by the photons absorbed by both materials in the composite.

$$\text{Semiconductor} + h\nu \rightarrow e^- + h^+ \quad (6)$$

During visible light irradiation, both g-C_3N_4 and α-Fe_2O_3 would absorb photons, that can generate electrons in CB and at the same time holes are populated in the VB. The electrons of the CB of g-C_3N_4 migrate to the CB of α-Fe_2O_3 due to less negativity, while the holes in the VB of α-Fe_2O_3 shifted to the VB in the g-C_3N_4. Thus, would prevent the recombination of photoexcited electrons and holes on both surfaces. The difference in the band edges of the hybrid α-Fe_2O_3/g-C_3N_4 composite have the ability to increase the quantity and stability of photogenerated charge carriers [40]. Consequently, more elections are formed in the CB of g-C_3N_4, and more holes are formed in the VB of α-Fe_2O_3, which increases the number of active species of $^{\bullet}O_2^-$ and $^{\bullet}OH$, respectively. Simultaneously, the accumulation of electrons in the CB of g-C_3N_4 participate in the photodegradation, while the holes generated in the VB of α-Fe_2O_3 participate in the formation of reactive species of $^{\bullet}OH$. Both the photocatalytic processes of the charge carriers must present a Z-scheme path. Accordingly, the photocatalytic degradation of toluene is increased when compared to the single prepared pure g-C_3N_4 and pure α-Fe_2O_3.

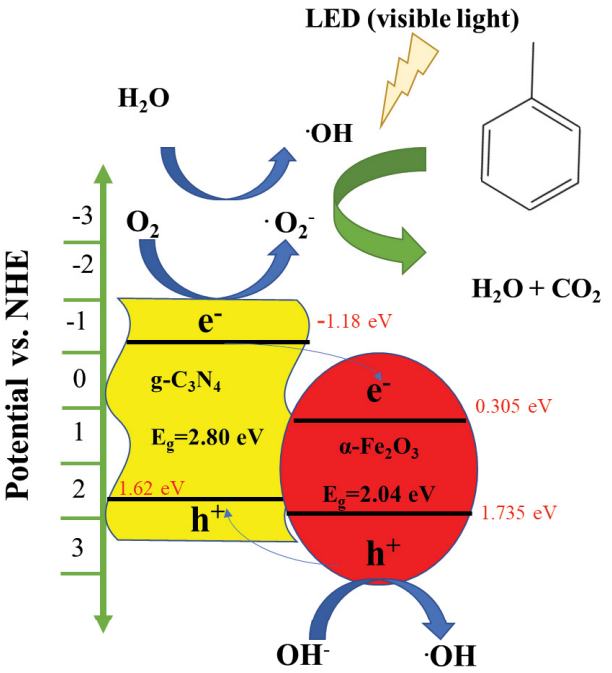

Fig. 10. A proposed Z-scheme for photocatalytic degradation of toluene over the α-Fe_2O_3/g-C_3N_4 composite under visible light irradiation.

4. Conclusion

In summary, this study presents the successful synthesis of α-Fe_2O_3 microspheres coupled with g-C_3N_4 to form a α-Fe_2O_3/g-C_3N_4 composite through the solvothermal process and proposes a Z-scheme of the photocatalytic mechanism. The coupling was validated by different instrumental methods such as: XRD, SEM, TEM, EDX, and PL measurements. Furthermore, the XPS and UV-Vis DRS combined data were used to analyze the pathway to produce more charge carriers during the photocatalysis procedure. All the prepared samples were tested for the degradation of toluene under visible light irradiation. Among all the prepared composites, the 60% α-Fe_2O_3/g-C_3N_4 composite showed excellent performance for the toluene degradation when compared to the uncoupled samples due to the narrowing the band gap up to 2.44 eV, therefore the charge carriers would be enhanced and reduced the electron-hole recombination rate.

Acknowledgements

One of the authors Said Al Mamari gratefully acknowledges Ministry of Education, Sultanate of Oman for the support. All the authors acknowledge Mr. Dr. Myo Tay Zar Myint, Surface Science Lab, Department of Physics, College of Science, Sultan Qaboos University and The Central Analytical and Applied Research Unit (CAARU) College of Science, Sultan Qaboos University, Oman.

References

[1] Y.P. Li, F.T. Li, X.J. Wang, J. Zhao, J.N. Wei, Y.J. Hao, Y. Liu, Z-scheme electronic transfer of quantum-sized α-Fe_2O_3 modified g-C_3N_4 hybrids for enhanced photocatalytic hydrogen production, Int. J. Hydrogen Energy, 42 (2017) 28327–28336.
[2] A. Umar, M.S. Akhtar, M.S. Al-Assiri, A.E. Al-Salami, S.H. Kim, Composite CdO-ZnO hexagonal nanocones: efficient materials for photovoltaic and sensing applications, Ceram. Int., 44 (2018) 5017–5024.
[3] M.J. Kang, H. Yu, W. Lee, H.G. Cha, Efficient Fe_2O_3/Cg-C_3N_4 Z-scheme heterojunction photocatalyst prepared by facile one-step carbonizing process, J. Phys. Chem. Solids, 130 (2019) 93–99.
[4] D. Hao, Y. Liu, S. Gao, H. Arandiyan, X. Bai, Q. Kong, J.B. Ni, Emerging artificial nitrogen cycle processes through novel

electrochemical and photochemical synthesis, Mater. Today, 46 (2021) 212–233.
[5] S. Kamal, S. Balu, S. Palanisamy, K. Uma, V. Velusamy, T.C. Yang, Synthesis of boron doped C_3N_4/$NiFe_2O_4$ nanocomposite: an enhanced visible light photocatalyst for the degradation of methylene blue, Results Phys., 12 (2019) 1238–1244.
[6] S. Ghattavi, A. Nezamzadeh-Ejhieh, A visible light driven AgBr/g-C_3N_4 photocatalyst composite in methyl orange photodegradation: focus on photoluminescence, mole ratio, synthesis method of g-C_3N_4 and scavengers, Composites, Part B, 183 (2020) 107712, doi: 10.1016/j.compositesb.2019.107712.
[7] T.D. Pham, B.K. Lee, Selective removal of polar VOCs by novel photocatalytic activity of metals co-doped TiO_2/PU under visible light, Chem. Eng. J., 307 (2017) 63–73.
[8] R. Sun, Q. Shi, M. Zhang, L. Xie, J. Chen, X. Yang, W. Zhao, Enhanced photocatalytic oxidation of toluene with a coral-like direct Z-scheme $BiVO_4$/g-C_3N_4 photocatalyst, J. Alloys Compd., 714 (2017) 619–626.
[9] S. Sun, C. Ji, L. Wu, S. Chi, R. Qu, Y. Li, Z. Xue, Facile one-pot construction of α-Fe_2O_3/g-C_3N_4 heterojunction for arsenic removal by synchronous visible light catalysis oxidation and adsorption, Mater. Chem. Phys., 194 (2017) 1–8.
[10] S.-M. Lam, J.-C. Sin, A.R. Mohamed, A review on photocatalytic application of g-C_3N_4/semiconductor (CNS) nanocomposites towards the erasure of dyeing wastewater, Mater. Sci. Semicond. Process., 47 (2016) 62–84.
[11] W. Zhang, C. Xu, E. Liu, J. Fan, X. Hu, Facile strategy to construction Z-scheme $ZnCo_2O_4$/g-C_3N_4 photocatalyst with efficient H_2 evolution activity, Appl. Surf. Sci., 515 (2020) 146039, doi: 10.1016/j.apsusc.2020.146039.
[12] D. Hao, C. Liu, X. Xu, M. Kianinia, I. Aharonovich, X. Bai, J.B. Ni, Surface defect-abundant one-dimensional graphitic carbon nitride nanorods boost photocatalytic nitrogen fixation, New J. Chem., 44 (2020) 20651–20658.
[13] D. Hao, J. Ren, Y. Wang, H. Arandiyan, M. Garbrecht, X. Bai, J.B. Ni, A green synthesis of Ru modified g-C_3N_4 nanosheets for enhanced photocatalytic ammonia synthesis, Energy Mater. Adv., 2021 (2021) 9761263, doi: 10.34133/2021/9761263.
[14] J. Li, Y. Liu, H. Li, C. Chen, Fabrication of g-C_3N_4/TiO_2 composite photocatalyst with extended absorption wavelength range and enhanced photocatalytic performance, J. Photochem. Photobiol., 317 (2016) 151–160.
[15] P.Y. Kuang, Y.Z. Su, G.F. Chen, Z. Luo, S.Y. Xing, N. Li, Z.Q. Liu, g-C_3N_4 decorated ZnO nanorod arrays for enhanced photoelectrocatalytic performance, Appl. Surf. Sci., 358 (2015) 296–303.
[16] S. Balu, S. Velmurugan, S. Palanisamy, S.W. Chen, V. Velusamy, T.C. Yang, E.S.I. El-Shafey, Synthesis of α-Fe_2O_3 decorated g-C_3N_4/ZnO ternary Z-scheme photocatalyst for degradation of tartrazine dye in aqueous media, J. Taiwan Inst. Chem. Eng., 99 (2019) 258–267.
[17] J.-C. Wang, L. Zhang, W.-X. Fang, J. Ren, Y.-Y. Li, H.-C. Yao, J.-S. Wang, Z.-J. Li, Enhanced photoreduction CO_2 activity over direct Z-scheme α-Fe_2O_3/Cu_2O heterostructures under visible light irradiation, ACS Appl. Mater. Interfaces, 7 (2015) 8631–8639.
[18] M. Hjiri, Highly sensitive NO_2 gas sensor based on hematite nanoparticles synthesized by sol–gel technique, J. Mater. Sci.: Mater. Electron., 31 (2020) 5025–5031.
[19] Y. Zhang, Y.A. Thomas, M. Antonietti, X. Wang, Activation of carbon nitride solids by protonation: morphology changes, enhanced ionic conductivity, and photoconduction experiments, J. Am. Chem. Soc., 131 (2009) 50–51.
[20] F. Dong, L. Wu, Y. Sun, M. Fu, Z. Wu, S.C. Lee, Efficient synthesis of polymeric g-C_3N_4 layered materials as novel efficient visible light driven photocatalysts, J. Mater. Chem., 21 (2011) 15171–15174.
[21] J. Liu, Y. Zhang, L. Lu, G. Wu, W. Chen, Self-regenerated solar-driven photocatalytic water-splitting by urea derived graphitic carbon nitride with platinum nanoparticles, Chem. Commun., 48 (2012) 8826–8828.
[22] Y. Xu, M.A. Schoonen, The absolute energy positions of conduction and valence bands of selected semiconducting minerals, Am. Mineral., 85 (2000) 543–556.
[23] N. Raeisi-Kheirabadi, A. Nezamzadeh-Ejhieh, A Z-scheme g-C_3N_4/Ag_3PO_4 nanocomposite: Its photocatalytic activity and capability for water splitting, Int. J. Hydrogen Energy, 45 (2020) 33381–33395.
[24] K. Uma, N. Arjun, G.T. Pan, T C.K. Yang, The photodeposition of surface plasmon Ag metal on SiO_2@α-Fe_2O_3 nanocomposites sphere for enhancement of the photo-Fenton behavior, Appl. Surf. Sci., 425 (2017) 377–383.
[25] F. Wang, Y. Feng, P. Chen, Y. Wang, Y. Su, Q. Zhang, G. Liu, Photocatalytic degradation of fluoroquinolone antibiotics using ordered mesoporous g-C_3N_4 under simulated sunlight irradiation: kinetics, mechanism, and antibacterial activity elimination, Appl. Catal., B, 227 (2018) 114–122.
[26] X. Yan, R. Xu, J. Guo, X. Cai, D. Chen, L. Huang, S. Tan, Enhanced photocatalytic activity of Cu_2O/g-C_3N_4 heterojunction coupled with reduced graphene oxide three-dimensional aerogel photocatalysis, Mater. Res. Bull., 96 (2017) 18–27.
[27] D. Li, J. Zan, L. Wu, S. Zuo, H. Xu, D. Xia, Heterojunction tuning and catalytic efficiency of g-C_3N_4–Cu_2O with glutamate, Ind. Eng. Chem. Res., 58 (2019) 4000–4009.
[28] A. Rufus, N. Sreeju, D. Philip, Synthesis of biogenic hematite (α-Fe_2O_3) nanoparticles for antibacterial and nanofluid applications, RSC Adv., 6 (2016) 94206–94217.
[29] F.T.L. Muniz, M.A.R. Miranda, C. Morilla dos Santos, J.M. Sasaki, The Scherrer equation and the dynamical theory of X-ray diffraction, Acta Crystallogr., Sect. A: Found. Crystallogr., 72 (2016) 385–390.
[30] W. Ning, T. Wang, H. Chen, X. Yang, Y. Jin, The effect of Fe_2O_3 crystal phases on CO_2 hydrogenation, PLoS One, 12 (2017) e0182955, doi: 10.1371/journal.pone.0182955.
[31] L. Lu, G. Wang, M. Zou, J. Wang, J. Li, Effects of calcining temperature on formation of hierarchical TiO_2/g-C_3N_4 hybrids as an effective Z-scheme heterojunction photocatalyst, Appl. Surf. Sci., 441 (2018) 1012–1023.
[32] F. Zhang, X. Li, Q. Zhao, Q. Zhang, M. Tadé, S. Liu, Fabrication of α-Fe_2O_3/In_2O_3 composite hollow microspheres: a novel hybrid photocatalyst for toluene degradation under visible light, J. Colloid Interface Sci., 457 (2015) 18–26.
[33] J. Tauc, R. Grigorovici, A. Vancu, Optical properties and electronic structure of amorphous germanium, Phys. Status Solidi B, 15 (1966) 627–637.
[34] D. Xiao, K. Dai, Y. Qu, Y. Yin, H. Chen, Hydrothermal synthesis of α-Fe_2O_3/g-C_3N_4 composite and its efficient photocatalytic reduction of Cr(VI) under visible light, Appl. Surf. Sci., 358 (2015) 181–187.
[35] T. Montalvo-Herrera, D. Sánchez-Martínez, D.B. Hernandez-Uresti, E. Zarazua-Morin, Facile preparation of $KBiO_3$/g-C_3N_4 composites with microwave irradiation for photocatalytic hydrogen production, J. Chem. Technol. Biotechnol., 94 (2019) 3440–3446.
[36] A.E.A. Bakr, W.M. El Rouby, M.D. Khan, A.A. Farghali, B. Xulu, N. Revaprasadu, Synthesis and characterization of Z-scheme α-Fe_2O_3 NTs/ruptured tubular g-C_3N_4 for enhanced photoelectrochemical water oxidation, J. Sol. Energy, 193 (2019) 403–412.
[37] W. Liu, L. Qiao, A. Zhu, Y. Liu, J. Pan, Constructing 2D BiOCl/C_3N_4 layered composite with large contact surface for visible-light-driven photocatalytic degradation, Appl. Surf. Sci., 426 (2017) 897–905.
[38] X. She, J. Wu, H. Xu, J. Zhong, Y. Wang, Y. Song, P.M. Ajayan, High efficiency photocatalytic water splitting using 2D α-Fe_2O_3/g-C_3N_4 Z-scheme catalysts, Adv. Energy Mater., 7 (2017) 1700025, doi: 10.1002/aenm.201700025.
[39] Y. Su, P. Chen, F. Wang, Q. Zhang, T. Chen, Y. Wang, K. Yao, W. Lv, G. Liu, Decoration of TiO_2/gC_3N_4 Z-scheme by carbon dots as a novel photocatalyst with improved visible-light photocatalytic performance for the degradation of enrofloxacin, RSC Adv., 7 (2017) 34096–34103.
[40] K.C. Christoforidis, T. Montini, E. Bontempi, S. Zafeiratos, J.J.D. Jaén, P. Fornasiero, Synthesis and photocatalytic application of visible-light active β-Fe_2O_3/g-C_3N_4 hybrid nanocomposites, Appl. Catal., B, 187 (2016) 171–180.